Nano Energy 148 (2026) 111632

Contents lists available at ScienceDirect

Nano Energy

journal homepage: www.elsevier.com/locate/nanoen

Perturbing *d*-band center via high-entropy modulation within spinel lattices toward enhanced oxygen evolution reaction catalysis

Jiwoo Song [a,1], Ramesh Kumar Chitumalla [b,1], Myung Hwa Kim [a,c,*], Joonkyung Jang [b,**], Dasol Jin [d,**]

[a] Department of Chemistry and Nanoscience, Ewha Womans University, Seoul 03760, Republic of Korea
[b] Department of Nanoenergy Engineering, Pusan National University, Busan 46241, Republic of Korea
[c] Institute of Multiscale Matter and System (IMMS), Ewha Womans University, Seoul 03760, Republic of Korea
[d] Department of Chemistry, Jeonbuk National University, Jeonju 54896, Republic of Korea

ARTICLE INFO

Keywords:
High-entropy
Oxygen evolution reaction
Formation energy
Adsorption evolution mechanism

ABSTRACT

With a multimetallic composition featuring diverse oxidation states and coordination environments, high-entropy oxides (HEOs) provide tunable affinities toward oxygen intermediates, thereby alleviating the intrinsic kinetic barriers of oxygen evolution reaction (OER). This compositional and structural diversity allows modulation of the reaction pathway and reduction of the activation barrier for the inherently sluggish four-electron OER process. Herein, we report the synthesis of a nanobelt-shaped, single-phase pentametallic spinel oxide $(Co_{1.8}Cr_{0.3}Rh_{0.3}Fe_{0.3}Ni_{0.3})O_4$ as an entropy-engineered electrocatalysts with tunable electronic structures for efficient OER. The multimetallic synergy upshifts the metal *d*-band center toward the Fermi level, optimizing oxygen intermediate binding and thereby reducing the OER overpotential. Compared to commercial IrO_2 in 1 M KOH, the spinel oxide exhibits a lower overpotential (1.58 V *vs.* RHE at 10 mA cm^{-2}), a smaller Tafel slope (66.1 mV dec^{-1}) and excellent durability maintaining stable performance over 12 h. These results highlight the potential of high-entropy spinel oxides, rationally engineered through multimetallic design, to achieve superior OER activity by finely tuning adsorption energetics and mitigating kinetic limitations.

1. Introduction

High-entropy oxides (HEOs) are multicomponent materials in which five or more metallic elements are homogeneously distributed within a single crystalline lattice [1]. The synergistic interaction among multiple metal constituents induces local lattice distortion and electronic redistribution, thereby generating a high density of catalytically active sites; this structural modulation alters bond lengths and electron-cloud distributions, which in turn govern the adsorption energies of key intermediates (*e.g.*, OH^- or H^+) during heterogeneous electrochemical reactions such as the oxygen and hydrogen evolution reactions [2]. At present, various synthetic strategies have been developed for the preparation of HEOs with rock-salt [3], perovskite [4], and spinel-type crystal structures [5,6]. These studies demonstrate that constituent elements exhibit distinct diffusion behaviors, thereby identifying diverse rate-limiting species and endowing HEOs with enhanced corrosion resistance and electrochemical stability. From this perspective, high-entropy spinel oxides (HESOs) have emerged as highly attractive candidates for OER catalysis due to the structural versatility of the AB_2O_4 lattice, which enables incorporation of diverse metal cations into tetrahedral (A) and octahedral (B) sites [7]. This structural flexibility enables precise tuning of active sites; especially, Co- and Fe-based spinel oxides (*e.g.*, $Co_xM_{3-x}O_4$ and $Fe_xM_{3-x}O_4$, where M = Ni [8,9], Cu [10] or Mn [8,11]) typically follow the adsorbate evolution mechanism (AEM), which involves four concerted proton–electron transfer steps on the oxide surface. The presence of different metal cations in the spinel lattice significantly affects the adsorption behavior and reaction kinetics of oxygen intermediates (*e.g.*, OH* and OOH*) [6]. Therefore, compositional tuning of spinel, particularly through the controlled occupation of octahedral sites by redox-active metal centers and modulation of metal oxygen covalency within redox active building blocks, serves as an effective strategy to tailor the reaction pathway and enhance OER

* Corresponding author at: Department of Chemistry and Nanoscience, Ewha Womans University, Seoul 03760, Republic of Korea.
** Corresponding authors.
E-mail addresses: myungkim@ewha.ac.kr (M.H. Kim), jkjang@pusan.ac.kr (J. Jang), dasoljin@jbnu.ac.kr (D. Jin).
[1] Equally contributed to this work

https://doi.org/10.1016/j.nanoen.2025.111632
Received 12 October 2025; Received in revised form 10 November 2025; Accepted 29 November 2025
Available online 1 December 2025

efficiency.

The OER is a key half-reaction in water splitting [12,13] and rechargeable metal–air batteries [14]; however, its inherently sluggish kinetics remain the principal bottleneck of the overall water-splitting process, serving as the major source of energy loss. Among the proposed mechanistic pathways, AEM is widely recognized as the predominant route under alkaline conditions, wherein the metal centers act as the primary redox-active sites [15]. In this mechanism, OER proceeds through four sequential concerted proton–electron transfer steps where surface-bound intermediates (OH*, O* and OOH*) are adsorbed, transformed, and ultimately evolve into O_2 [16]. The catalytic reactivity is largely dictated by the adsorption strength and subsequent transformation of these intermediates [17], wherein the potential-determining step (PDS), corresponding to the elementary step with the highest free-energy barrier, determines the theoretical overpotential [18,19]. Governed by the interplay between the applied potential and the competing reaction kinetics, the established scaling relationship ($\Delta G_{OOH^*} = \Delta G_{OH^*} + 3.2$ eV) reflects the intrinsic limitation in concurrently optimizing the adsorption energies of OH* and OOH* [20], thereby impeding the rational design of catalysts that exhibit both high activity and low overpotential. To overcome this limitation, numerous strategies such as heteroatom substitution [21], vacancy engineering [22] and alloying [23] have been employed to tailor the electronic structure of OER catalysts. Multimetallic oxides, especially HESOs [24–26], provide a versatile platform in which the incorporation of multiple transition metals not only tunes the electronic structure but also modulates local coordination environments. These synergistic effects can optimize intermediate adsorption and reduce the PDS energy barrier, thereby lowering the overall overpotential [27].

In this study, we investigate the alkaline OER mechanism on representative spinel oxide surfaces with particular emphasis on the (311) facet of $(Co_{1.8}Cr_{0.3}Rh_{0.3}Fe_{0.3}Ni_{0.3})O_4$. The tunable physicochemical properties of these materials, arising from the distribution of multiple transition metal ions across tetrahedral and octahedral coordination sites, enable modulation of adsorption energies and reduction of the activation energy barrier. By integrating density functional theory calculations with electrochemical characterization, we elucidate the elementary step of the AEM and identify the PDS under alkaline conditions. The as-prepared HESOs exhibit a significantly lower overpotential than the commercial IrO_2 benchmark with the PDS identified as the conversion of OH* into O*. This process modulates the Fermi level through an upshift of the *d*-band center within the combined metal composition, thereby enhancing the orbital overlap between the metal *d*-states and oxygen *p*-states.

2. Experimental

2.1. Materials

Cobalt (II) chloride ($CoCl_2$), chromium (III) chloride hexahydrate ($CrCl_3 \bullet 6\ H_2O$), iron (III) chloride hydrate ($FeCl_3 \bullet xH_2O$), rhodium (III) chloride hydrate ($RhCl_3 \bullet xH_2O$), nickel (II) chloride hexahydrate ($NiCl_2 \bullet 6\ H_2O$), poly(vinylpyrrolidone) (PVP, MW ≈ 1 300 000), iridium oxide (IrO_2, nanoparticle), potassium hydroxide (KOH) and Nafion (5 wt % solution) were purchased from Sigma-Aldrich (St. Louis, MO, USA). N, N-dimethylformamide (DMF, extra pure grade) and ethanol (94.5 %, extra pure grade) were purchased from Ducksan (Korea). All other chemicals used were of analytical grade without further purification, and all solutions used for experiments were prepared with deionized water (resistivity ≥ 18 MΩ cm).

2.2. Synthesis

A pentametallic high-entropy spinel oxide, $(Co_{1.8}Cr_{0.3}Rh_{0.3}Fe_{0.3}Ni_{0.3})O_4$, was synthesized *via* electrospinning followed by post-annealing. First, total of 80 mg of metal precursors were dissolved in 1:1 (*v*/*v*) mixture of DMF and ethanol. The molar ratio of the metal ions was fixed at 6:1:1:1:1 for Co:Cr:Rh:Fe:Ni, respectively. The resulting solution was ultrasonicated for 30 min and then stirred in 60 °C water bath for 10 min. Subsequently, 327.3 mg of PVP was added, and the mixture was stirred at 50 °C for 48 h to ensure complete homogenization and viscosity optimization for electrospinning. As-prepared solution was then loaded into 12 mL plastic syringe fitted with 21-gauge needle. Electrospinning (NanoNC ESR200R2) was performed under the following conditions: flow rate of 12 μL min^{-1}, applied voltage of 12.5 kV and a needle-to-collector distance of 12 cm. The resulting as-spun nanofibers were calcined at 600 °C for 1 h under the gas flow of 10 sccm O_2 and 80 sccm He. For comparison, $(Co_{2.1}Cr_{0.3}Rh_{0.3}Fe_{0.3})O_4$ and $(Co_{2.4}Cr_{0.3}Rh_{0.3})O_4$ were synthesized following the same procedure with the only variation being the absence of Ni and Ni/Fe precursors, respectively.

2.3. Physical characterization

Crystal structure was analyzed by X-ray diffraction (XRD, Rigaku D/Max-2000/PC) using Cu Kα radiation. Morphological and elemental analyses were conducted *via* field-emission scanning electron microscopy (FE-SEM, JEOL JSM-7610F) equipped with energy-dispersive X-ray spectroscopy (EDS). High-resolution structural features were examined using high-resolution transmission electron microscopy (HRTEM, FEI Tecnai F20) and transmission electron microscopy (TEM, JEOL JEM-ARM200F NEOARM) coupled with EDS (JEOL JED-2300T). Surface chemical states were investigated by angle resolved X-ray photoelectron spectroscopy (AR-XPS, Thermo Fisher Scientific K-ALPHA XPS, Al Kα radiation at 12 kV) and vibrational properties were probed using Raman microscope (HORIBA LabRAM HR Evolution 800).

2.4. Computational calculation

All simulations were carried out using the Vienna Ab initio Simulation Package (VASP 6.3.2) [28–30], which solves the Kohn-Sham equations within the framework of density functional theory (DFT) under periodic boundary conditions. The exchange-correlation functional employed in this study was the Perdew–Burke–Ernzerhof (PBE) functional [31], a generalized gradient approximation (GGA) and all simulations were spin-polarized. Long-range dispersion interactions were accounted for using Grimme's DFT-D3 semi-empirical method [32] with Becke-Johnson damping [33,34] to improve the accuracy of the dispersion correction. Structural optimizations of the atomic positions were performed using a quasi-Newton algorithm, specifically a conjugate gradient algorithm, with geometries optimized until the maximum energy difference between successive ionic steps was less than 10^{-5} eV and the Hellmann-Feynman forces on each atom were reduced below 0.02 eV/Å. The interaction between core and valence electrons was treated using the projected augmented wave (PAW) method [35], with PAW pseudopotentials employed to describe ionic cores. The valence electron configurations used for O, Co, Cr, Fe, Ni and Rh were 2s2p, 3d4s, 3d4s, 3d4s, 3d4s and 4d5s, respectively. To determine the plane-wave energy cutoff, we performed energy convergence tests, and a plane-wave kinetic energy cutoff of 500 eV was found to be sufficient for an accurate description of the electrocatalysts studied. In reciprocal space, Monkhorst–Pack [36] *k*-point sampling of the Brillouin zone was employed, using a 1 × 1 × 1 *k*-point grid for all simulations. Further details of the computational calculations are provided in Supporting Information.

2.5. Electrodes and electrochemical measurement

To evaluate the electrochemical properties, as-prepared nanomaterials were dispersed in deionized water at a concentration of 2 mg mL^{-1}. For each sample, 5 μL of the dispersion was drop-cast onto a polished glassy carbon (GC) rotating disk electrode (RDE) and dried in

an oven at 60 °C for 10 min. This process was repeated six times to achieve a total catalyst loading of 60 μg. Subsequently, 10 μL of 0.1 wt% Nafion solution (diluted in ethanol) was applied as a binder and then dried in a desiccator for 30 min. Prior to catalyst loading, all GC electrodes were polished with an alumina slurry on a wet polishing cloth and ultrasonicated in deionized water for 5 min to remove residue. Electrochemical measurements were conducted in a three-electrode setup, using the catalyst-coated GC electrode as the working electrode, a saturated calomel electrode (SCE) as the reference electrode and a coiled platinum wire as the counter electrode. Current densities were normalized to the geometric surface area (GSA) of the electrode, which was determined by chronocoulometry (CC) in 0.1 M KCl solution containing 10 mM $Ru(NH_3)_6Cl_3$ as redox probe. All electrochemical experiments were carried out in Ar-saturated 1 M KOH aqueous solution using an electrochemical analyzer (CHI 730D, CH instrument, Inc.) with RDE (RDE-1 rotor/Epsilon electrochemical analyzed, BASi). AC electrochemical impedance spectroscopy (EIS) measurements were performed in 1 M KOH (*aq*) at potentials corresponding to an OER current density of 10 mA cm^{-2} for each electrocatalyst over a frequency range of 1 Hz to 10 kHz. The *i*R drop in the three-electrode configuration was automatically compensated.

3. Results and discussion

3.1. Physical characterization

The pentametallic high-entropy spinel oxide, $(Co_{1.8}Cr_{0.3}Rh_{0.3}Fe_{0.3}Ni_{0.3})O_4$, synthesized *via* electrospinning followed by post-annealing, exhibited a nanobelt-like morphology as revealed by TEM analysis (Fig. 1a). The resulting nanobelts with surface bumps exhibit an average width of approximately 393 nm, similar to those of the ternary and quaternary counterparts (Fig. S1). Despite the incorporation of five metal components, the inverse FFT image in Fig. 1(b) reveals well-defined lattice fringes, indicative of a highly crystalline structure. The measured *d*-spacings correspond to the (110), (311) and (220) planes with values of 0.480, 0.303 and 0.256 nm, respectively, consistent with the standard spinel Co_3O_4 phase (JCPDS No. 42–1467). These results suggest that the as-prepared nanobelts are based on Co_3O_4-type spinel framework, in which Cr, Fe, Rh and Ni atoms are substitutionally incorporated during the annealing-induced crystallization process. Notably, all substituting cations, which have a similar ionic radius (*i.e.*, 0.061–0.067 nm for Fe^{3+}, Cr^{3+} and Rh^{3+}) [37], possess larger ionic radii than cobalt, likely contributing to the observed

lattice expansion relative to pristine Co_3O_4. EDS mapping images in Fig. 1(c,d) confirm the uniform distribution of all five metal elements

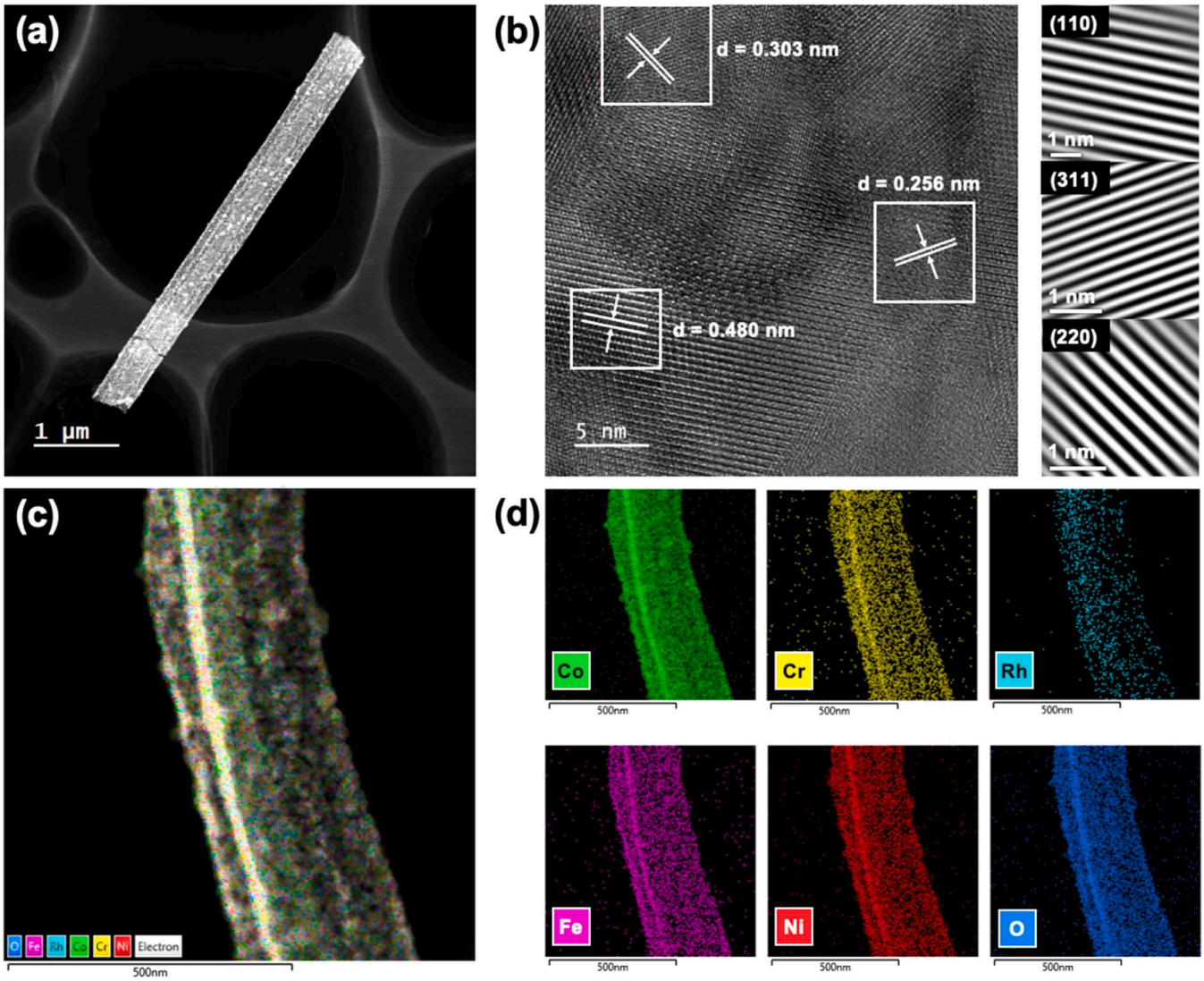

Fig. 1. TEM characterization of $(Co_{1.8}Cr_{0.3}Rh_{0.3}Fe_{0.3}Ni_{0.3})O_4$ nanobelts: (a) HAADF-STEM image and (b) HRTEM image with corresponding inverse FFT. (c) Overlaid EDS elemental mapping image and (d) corresponding elemental distribution maps for Co, Cr, Rh, Fe, Ni and O.

within the $(Co_{1.8}Cr_{0.3}Rh_{0.3}Fe_{0.3}Ni_{0.3})O_4$ nanobelts, indicating the absence of phase separation and suggesting the successful formation of a single-phase high-entropy spinel structure.

The electrospun nanomaterials exhibited a highly crystalline single-phase spinel oxide structure without any detectable secondary phases, as confirmed by XRD analysis (Fig. 2a). The patterns of the synthesized samples closely match that of standard Co_3O_4 (JCPDS No. 42–1467), confirming the formation of a spinel-phase structure. Crystallite sizes, determined using the Scherrer equation, range from 8.5 to 11 nm, indicating a uniform degree of crystallinity across all compositions (Table S1). The (311) diffraction peak, typically observed near 36°, shows a systematic shift toward lower angles with increasing multimetal substitution: 35.9° for $(Co_{2.4}Cr_{0.3}Rh_{0.3})O_4$, 35.4° for

$(Co_{2.1}Cr_{0.3}Rh_{0.3}Fe_{0.3})O_4$ and 35.0° for $(Co_{1.8}Cr_{0.3}Rh_{0.3}Fe_{0.3}Ni_{0.3})O_4$. These negative shifts in peak position indicate lattice expansion, which can be attributed to the progressive substitution of cobalt ions by other cations with larger ionic radii, thereby reducing the overall cobalt content within the lattice framework. SEM–EDS analysis in Fig. 2(b) confirms that the elemental compositions of the as-prepared spinel oxide series closely match the target molar ratios of metal precursors introduced during the electrospinning process (see *Experimental* section). The observed proportional incorporation of each metal element within the single-phase spinel structure supports the validity of the designated compositional formulas. Detailed atomic percentages for all samples are summarized in Table S2.

The surface chemical states of the constituent elements in $(Co_{1.8}Cr_{0.3}Rh_{0.3}Fe_{0.3}Ni_{0.3})O_4$ nanobelts were investigated using AR-XPS. The Co 2p spectrum (Fig. 2c) shows two well-defined spin-orbit doublets. Peaks at 781.0 eV ($2p_{3/2}$) and 795.7 eV ($2p_{1/2}$) correspond to Co^{2+}, while those at 778.9 eV and 794.5 eV are attributed to Co^{3+}, indicating the coexistence of both oxidation states. This is consistent with the characteristic electronic structure of Co_3O_4-type spinel oxides [38]. The Cr 2p spectrum (Fig. 2d) exhibits two dominant peaks at 575.6 eV ($2p_{3/2}$) and 585.3 eV ($2p_{1/2}$) with a spin-orbit splitting of

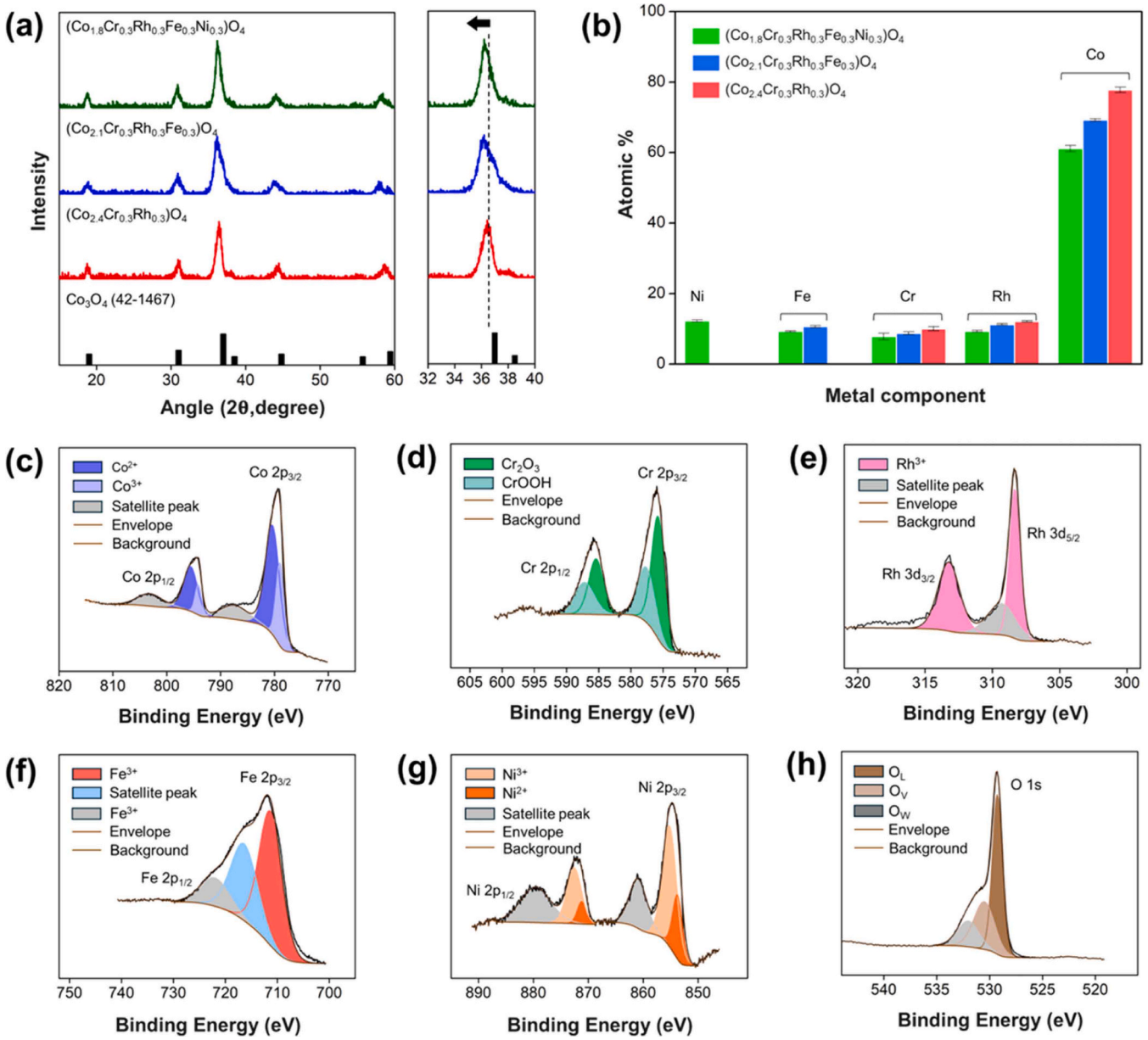

Fig. 2. (a) XRD patterns of $(Co_{1.8}Cr_{0.3}Rh_{0.3}Fe_{0.3}Ni_{0.3})O_4$, $(Co_{2.1}Cr_{0.3}Rh_{0.3}Fe_{0.3})O_4$, $(Co_{2.4}Cr_{0.3}Rh_{0.3})O_4$ and reference Co_3O_4 with an enlarged view of the (311) reflection around $2\theta = 36°$. (b) Comparison of elemental atomic ratios based on SEM–EDS analysis. AR-XPS spectra of $(Co_{1.8}Cr_{0.3}Rh_{0.3}Fe_{0.3}Ni_{0.3})O_4$ nanobelts for the (c) Co 2p, (d) Cr 2p, (e) Rh 3d, (f) Fe 2p, (g) Ni 2p and (h) O 1 s regions, respectively.

9.7 eV, confirming the presence of Cr^{3+} [39,40]. Additionally, two weaker peaks with similar splitting are observed, whose $2p_{3/2}$ to $2p_{1/2}$ area ratio (~1.7:1) is consistent with CrOOH, suggesting partial surface adsorption of OOH species onto Cr sites [39]. The Rh 3d spectrum (Fig. 2e) reveals $3d_{5/2}$ peak at 308.3 eV and $3d_{3/2}$ peak at 313.0 eV, both matching well with the Rh^{3+} oxidation state in Rh_2O_3 [41]. Similarly, the Fe 2p spectrum (Fig. 2f) shows peaks at 710.9 eV ($2p_{3/2}$) and 723.4 eV ($2p_{1/2}$), along with a characteristic shake-up satellite, indicating the presence of Fe^{3+} in a spinel lattice environment [42]. The Ni 2p spectrum (Fig. 2g) displays two spin-orbit doublets corresponding to Ni^{2+} and Ni^{3+}, along with two characteristic shake-up satellite peaks. The observed spin-orbit splitting (~17 eV) and peak positions are in good agreement with those reported for $NiCo_2O_4$-type spinel oxides where the predominant Ni^{2+} cations and a portion of the Co cations occupy octahedral sites, while the remaining Co^{3+} cations are located in tetrahedral sites [43]. Quantitative analysis based on normalized peak areas reveals that Ni^{2+} is the dominant oxidation state, with a Ni^{2+} to Ni^{3+} ratio of approximately 3:1. Finally, the O 1 s spectrum (Fig. 2h) is deconvoluted into three distinct peaks at 529.3 eV, 530.5 eV and 532.0 eV, corresponding to lattice oxygen (O^{2-}), oxygen vacancies and surface-adsorbed oxygen species, respectively [44]. These features are characteristic of spinel-type oxides, and further confirm the successful formation of a single-phase pentametallic spinel oxide structure in $(Co_{1.8}Cr_{0.3}Rh_{0.3}Fe_{0.3}Ni_{0.3})O_4$.

The Raman spectra of a series of spinel-type metal oxides are presented in Fig. S2. All three samples exhibit characteristic vibrational modes of spinel oxides, including the $A_{1\,g}$, $T_{2\,g}(2)$ and E_g modes. The $A_{1\,g}$ mode corresponds to symmetric oxygen stretching vibrations at the tetrahedral (T_d) A-site of the AB_2O_4 spinel structure [45], while the $T_{2\,g}(2)$ mode is attributed to asymmetric oxygen stretching vibrations associated with the octahedral (O_h) B-site [46]. The E_g mode originates from symmetric bending vibrations involving both T_d and O_h sites within the spinel lattice [47]. A progressive red shift of the $A_{1\,g}$ (650 → 631 cm^{-1}) and $T_{2\,g}(2)$ (532 → 519 cm^{-1}) modes is observed as compositional complexity increases from ternary to pentametallic spinel oxides, reflecting the enhanced distortion of the tetrahedral and octahedral coordination environments induced by the incorporation of additional transition-metal ions into the spinel lattice [48]. The E_g mode is also affected by the gradual substitution of Co with multi metal ions, which leads to a reduction in the overall structural symmetry; this decrease in symmetry is consistent with the corresponding changes observed in the vibrational features of the Raman spectra [49].

3.2. Computational calculation with electrochemical characterization

The OER activity of the as-prepared materials was evaluated in Ar-

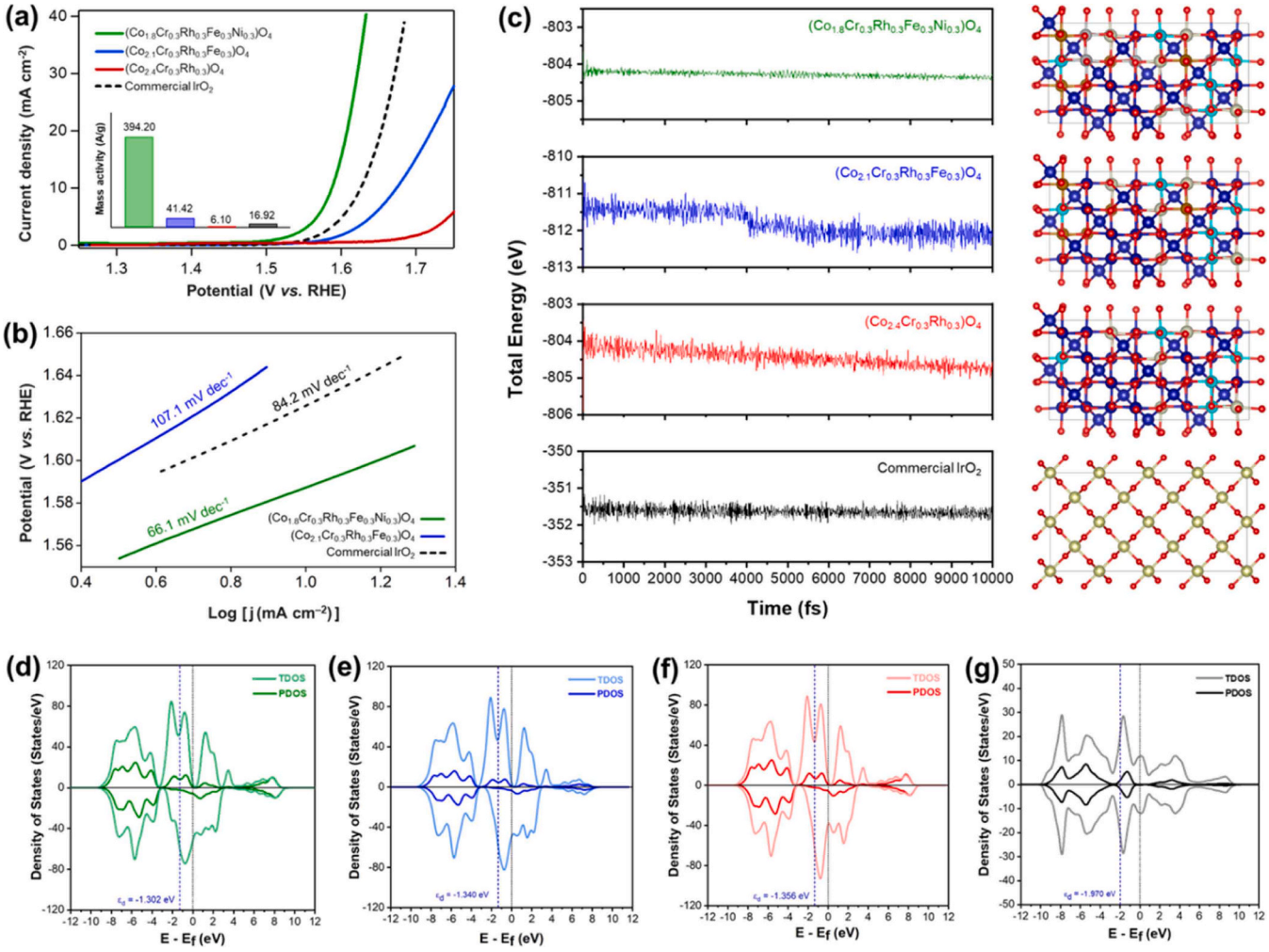

Fig. 3. (a) LSV curves of the as-prepared nanomaterials in Ar-purged 1 M KOH (*aq*) (inset: comparison of mass activities at 1.63 V) and (b) corresponding Tafel plots. (c) Ab initio molecular dynamics (AIMD) simulations showing total energy fluctuations over 10 000 fs at 300 K with representative crystal structures. All systems exhibit stable oscillations without significant drift, confirming the thermodynamic stability of the spinel oxides. Total and projected density of states (TDOS and PDOS) for (d) $(Co_{1.8}Cr_{0.3}Rh_{0.3}Fe_{0.3}Ni_{0.3})O_4$, (e) $(Co_{2.1}Cr_{0.3}Rh_{0.3}Fe_{0.3})O_4$, (f) $(Co_{2.4}Cr_{0.3}Rh_{0.3})O_4$ and (g) IrO_2. The calculated *d*-band centers (ε_d) are indicated by blue dashed lines and the Fermi level (E_f) is referenced at 0 eV (black dotted line).

purged 1 M KOH (*aq*) using a standard three-electrode configuration. As shown by the *i*R-corrected linear sweep voltammetry (LSV) curves (Fig. 3a), $(Co_{1.8}Cr_{0.3}Rh_{0.3}Fe_{0.3}Ni_{0.3})O_4$ exhibits the lowest potential of 1.58 V at the benchmark current density of 10 mA cm^{-2}, which is markedly lower than those of $(Co_{2.1}Cr_{0.3}Rh_{0.3}Fe_{0.3})O_4$ (1.67 V), $(Co_{2.4}Cr_{0.3}Rh_{0.3})O_4$ (1.77 V) and even commercial IrO_2 (1.63 V). When normalized by the mass of the noble metal component (Rh or Ir) at 1.63 V (inset of Fig. 3a), the pentametallic spinel oxide delivers the highest mass activity among all tested samples, surpassing even

that of commercial IrO_2. To further probe the reaction kinetics, Tafel slopes were derived from the LSV data according to the Tafel equation ($\eta = a + b \log j$, where η is the overpotential, b is the Tafel slope, and j is the current density) [50]. The pentametallic oxide displayed the lowest Tafel slope of 66.1 mV dec^{-1}, compared to 107.1 mV dec^{-1} for the tetrametallic counterpart and 84.2 mV dec^{-1} for IrO_2 (Fig. 3b). These results underscore that the high-entropy spinel oxide facilitates the most favorable reaction kinetics, thereby accelerating OER processes relative to both multi-component oxides with fewer elements and the commercial benchmark catalyst. To complement our experimental observations and elucidate the atomic-scale mechanisms underlying the improved OER kinetics, we performed first-principles-based DFT simulations. The theoretically determined *d*-band center shifts and the binding affinities of key oxygen intermediates on the surfaces of these novel multimetallic high-entropy catalysts demonstrate excellent corroboration with the experimental findings. By integrating multiple metallic elements, furthermore, the thermodynamic and kinetic stabilities of the three catalysts were systematically evaluated through formation energy calculations and AIMD simulations. The formation energies (E_f) were calculated using the following equations:

$$E_f = E_{Co_{28}Cr_5Rh_5Fe_5Ni_5O_{64}} - E_{Co_{48}O_{64}} + 20\mu_{Co} - 5\mu_{Cr} - 5\mu_{Rh} - 5\mu_{Fe} - 5\mu_{Ni} \quad (1)$$

$$E_F = E_{Co_{33}Cr_5Rh_5Fe_5O_{64}} - E_{Co_{48}O_{64}} + 15\mu_{Co} - 5\mu_{Cr} - 5\mu_{Rh} - 5\mu_{Fe} \quad (2)$$

$$E_F = E_{Co_{38}Cr_5Rh_5O_{64}} - E_{Co_{48}O_{64}} + 10\mu_{Co} - 5\mu_{Cr} - 5\mu_{Rh} \quad (3)$$

where Eq.(1) corresponds to $(Co_{1.8}Cr_{0.3}Rh_{0.3}Fe_{0.3}Ni_{0.3})O_4$, Eq.(2) to $(Co_{2.1}Cr_{0.3}Rh_{0.3}Fe_{0.3})O_4$ and Eq.(3) to $(Co_{2.4}Cr_{0.3}Rh_{0.3})O_4$. Compared to pristine Co_3O_4, the heteroatom-substituted spinel oxide series exhibited enhanced thermodynamic stability with formation energies of −131.34 meV/atom for $(Co_{1.8}Cr_{0.3}Rh_{0.3}Fe_{0.3}Ni_{0.3})O_4$, −211.07 meV/atom for $(Co_{2.1}Cr_{0.3}Rh_{0.3}Fe_{0.3})O_4$ and −146.96 meV/atom for $(Co_{2.4}Cr_{0.3}Rh_{0.3})O_4$, respectively. To further assess dynamic stability, we performed AIMD simulations on multimetallic catalyst systems and compared them with IrO_2. The total energy profiles of all four systems were monitored over a simulation period of 10,000 fs (Fig. 3c). The three modified spinel oxides exhibited only minor energy oscillations within a narrow range and showed no significant drift, confirming their dynamic stability. Analysis of the final simulation snapshots (right side of Fig. 3c) revealed that all structures maintained their crystallographic framework, confirming that the structural integrity was preserved under the applied simulation conditions.

A critical descriptor for evaluating the OER activity of the catalysts is the position of the *d*-band center relative to the Fermi level. According to the *d*-band theory, an upshift in the *d*-band center of transition metals exhibits reduced occupancy of antibonding states formed between the metal *d*-orbitals and adsorbate *p*-orbitals. This results in stronger binding of OER intermediates with the catalyst, thereby facilitating a more favorable reaction pathway and ultimately reducing the overpotential required for OER [51]. To probe this relationship, the electronic structures of the catalysts were analyzed through density of states (DOS) calculations. In particular, the influence of multimetallic composition on the position of the *d*-band center was evaluated to clarify its role in modulating the electronic structure and enhancing the catalytic activity toward the OER. The *d*-band center (ε_d) was calculated using the following formula:

$$\varepsilon_d = \frac{\int_{-\infty}^{\infty} n_d(\varepsilon)\varepsilon d\varepsilon}{\int_{-\infty}^{\infty} n_d(\varepsilon) d\varepsilon}$$

where, ε is the energy relative to the Fermi energy, and $n_d(\varepsilon)$ is the DOS projected onto the *d*-states. The calculated d-band centers are located at −1.302 eV for $(Co_{1.8}Cr_{0.3}Rh_{0.3}Fe_{0.3}Ni_{0.3})O_4$, −1.340 eV for $(Co_{2.1}Cr_{0.3}Rh_{0.3}Fe_{0.3})O_4$ and −1.356 eV for $(Co_{2.4}Cr_{0.3}Rh_{0.3})O_4$, respectively (Fig. 3d-f). These values are significantly upshifted relative to those of pristine Co_3O_4 (−1.432 eV; Fig. S3) and commercial IrO_2 (−1.970 eV; Fig. 3g). As the *d*-band center shifts closer to the Fermi level through elemental substitution, the interaction between metal sites and oxygen-based intermediates (O*, OH*, OOH*) is strengthened, optimizing their binding energies and facilitating more efficient OER kinetics. Our *d*-band center study reveals that the most pronounced upshift, observed in pentametallic spinel oxide, $(Co_{1.8}Cr_{0.3}Rh_{0.3}Fe_{0.3}Ni_{0.3})O_4$ (−1.302 eV), suggests an optimally tuned electronic structure for strong adsorbate interaction and, consequently, superior OER activity.

The OER mechanism proceeds through sequential adsorption and desorption of oxygenated intermediates. In heterostructures, the formation of built-in electric fields alters the local electron density, thereby regulating the adsorption behavior of the intermediates [15]. To elucidate the catalytic behavior of pentamentallic high-entropy spinel oxides, we examined the four-electron OER pathway. The adsorption configurations and Gibbs free energy changes of the key reaction intermediates were calculated according to the adsorbate evolution mechanism (AEM). The elementary electrochemical steps involved in the OER mechanism on the (311) surface of $(Co_{1.8}Cr_{0.3}Rh_{0.3}Fe_{0.3}Ni_{0.3})O_4$ were investigated under alkaline conditions (Fig. 4a). As the octahedral sites in spinel oxides are generally recognized as the dominant active centers for the OER, we selected the Co octahedral sites over the tetrahedral sites for our investigation [52]. The free energy profile reveals that the potential-determining step (PDS) is the conversion of OH* into O*, which exhibits the highest Gibbs free energy change of 1.61 eV among all reaction steps (Fig. 4b). This moderate energy barrier corresponds to an overpotential (η) of 0.38 V, demonstrating the intrinsic catalytic efficiency of the multimetallic spinel oxide toward the OER. The relatively low barrier for the PDS can be attributed to the optimized electronic structure resulting from multimetallic substitution. As demonstrated by the *d*-band analysis (*vide supra*), the upshift of the *d*-band center in $(Co_{1.8}Cr_{0.3}Rh_{0.3}Fe_{0.3}Ni_{0.3})O_4$ toward the Fermi level enhances the orbital overlap between the metal *d*-states and the oxygen *p*-states, thereby strengthening the adsorption of oxygenated intermediates. This balanced interaction ensures optimal binding strength and facilitates efficient charge transfer during the OER process. As a result, the catalyst demonstrates excellent durability, maintaining a nearly stable potential during 12 h of continuous OER operation at a constant current density of 10 mA cm^{-2} while the commercial electrocatalyst showed steep decay after 8 h (Fig. 4c). The stability of the electrocatalyst was further evaluated using electrochemical impedance spectroscopy (EIS) (Fig. 4d). Before the stability test, both samples exhibited comparable solution resistances of approximately 14 Ω; however, the charge-transfer resistance, which reflects the intrinsic conductivity and interfacial kinetics, was notably lower for the pentametallic spinel oxide. After long-term operation, this material maintained a low charge-transfer resistance of 123 Ω, in contrast to 210 Ω for commercial IrO_2, demonstrating superior electronic conductivity and faster charge-transfer behavior. Moreover, the spinel oxide showed minimal changes in both charge-transfer and solution resistances after continuous chronopotentiometric operation, whereas IrO_2 exhibited significant increases in both. These results indicate that the pentametallic spinel oxide possesses excellent structural integrity and electrochemical stability under prolonged operating conditions. Synergistic interactions among the multimetallic constituents tune the electronic structure of active sites, promoting faster charge

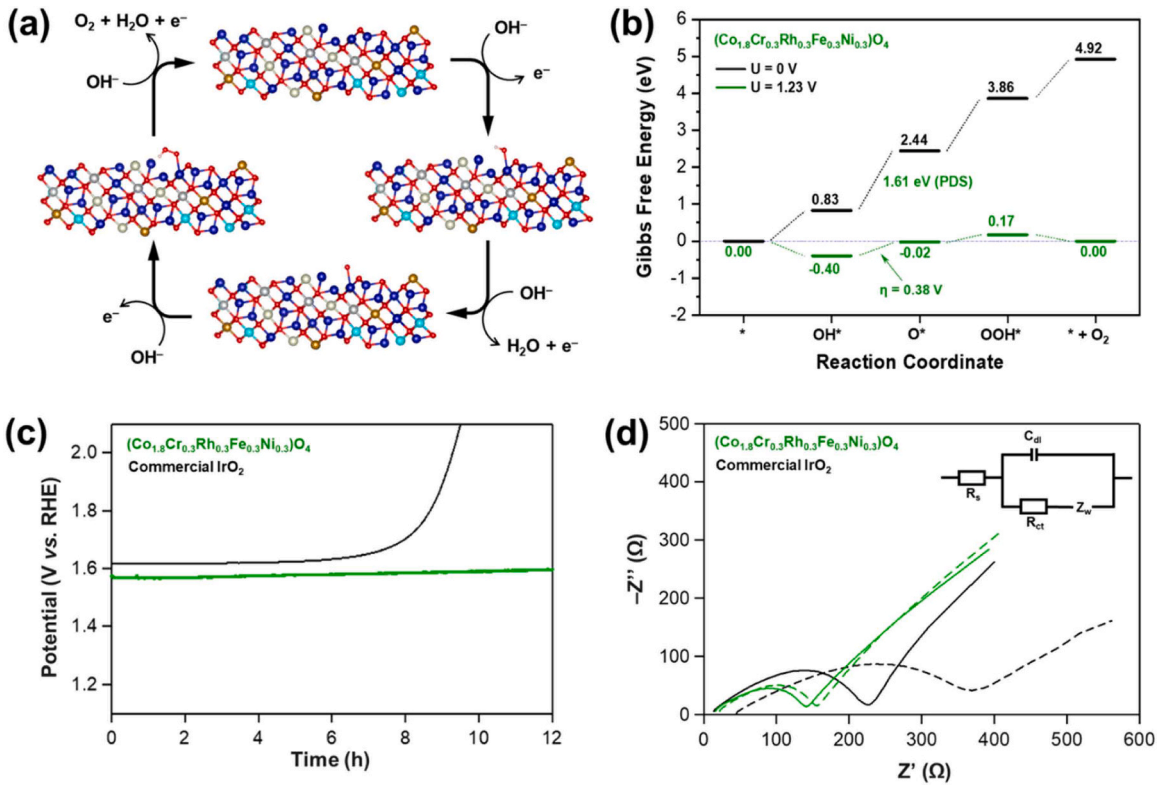

Fig. 4. (a) Optimized adsorption geometries of the key OER intermediates (OH*, O* and OOH*; clockwise) on the. (311) surface of $(Co_{1.8}Cr_{0.3}Rh_{0.3}Fe_{0.3}Ni_{0.3})O_4$. (b) Gibbs free energy (ΔG) profiles at applied potentials of 0 V (black). and 1.23 V (green) *vs.* RHE. The potential-determining step (PDS) is the formation of O* associated with a free energy. change of 1.61 eV corresponding to an overpotential (η) of 0.38 V. (c) Chronopotentiometry measurements recorded. at a constant current density of 10 mA cm^{-2} over 12 h. (d) EIS spectra recorded before (solid line) and after (dotted. line) chronopotentiometric measurement (inset: equivalent circuit model used in fitting).

transfer and lower overpotential, thus outperforming numerous state-of-the-art alkaline OER electrocatalysts (Table S3).

4. Conclusion

In this study, the pentametallic high-entropy spinel oxide $(Co_{1.8}Cr_{0.3}Rh_{0.3}Fe_{0.3}Ni_{0.3})O_4$ was successfully synthesized, exhibiting superior activity and durability toward alkaline OER. The unique structural and electronic configuration not only enhances charge transport but also promotes the formation of reactive oxygen species. The coexistence of multiple oxidation states and coordination environments, as supported by favorable formation energies and confirmed by AIMD simulations, endows the material with outstanding structural robustness. This compositional heterogeneity facilitates alternative reaction pathways during the OER, resulting in a low overpotential of 1.58 V at 10 mA cm^{-2} and a Tafel slope of 66.1 mV dec^{-1}, outperforming the commercial IrO_2 catalyst (1.63 V and 84.2 mV dec^{-1}). Electronic structure analysis further reveals an upshift of the d-band center toward the Fermi level, which strengthens orbital hybridization between metal *d*-states and oxygen *p*-states, enhancing adsorption of oxygenated intermediates. Moreover, long-term potentiometric measurements confirm superior electrochemical stability, as evidenced by the nearly unchanged potential over 12 h continuous operation, whereas IrO_2 exhibited a pronounced potential decay. Therefore, the integration of high configurational entropy and synergistic multi-cation effects positions $(Co_{1.8}Cr_{0.3}Rh_{0.3}Fe_{0.3}Ni_{0.3})O_4$ as an efficient and durable electrocatalyst for OER.

Author Contributions

D.J., M.H.K., and J.J. supervised the research. J.S. and R.K.C. performed the experiments and analyzed the data. D.J., J.S., and R.K.C. curated results and co-wrote the manuscript. D.J. and J.S. revised the manuscript. All authors discussed the results and contributed to the final version of the manuscript.

CRediT authorship contribution statement

Joonkyung Jang: Writing – original draft, Supervision, Software, Resources, Project administration, Investigation, Funding acquisition. **Ramesh Kumar Chitumalla:** Visualization, Software, Methodology, Investigation, Formal analysis, Data curation, Writing – original draft. **Jiwoo Song:** Writing – original draft, Visualization, Validation, Methodology, Formal analysis, Data curation. **Myung Hwa Kim:** Writing – original draft, Validation, Supervision, Resources, Project administration, Methodology, Funding acquisition. **Dasol Jin:** Writing – review & editing, Writing – original draft, Validation, Supervision, Methodology, Investigation, Conceptualization, Funding acquisition, Project administration.

Declaration of Competing Interest

The authors declare that they have no known competing financial interests or personal relationships that could have appeared to influence the work reported in this paper.

Acknowledgements

This work was financially supported by the National Research Foundation of Korea (NRF) funded by the Ministry of Science and ICT or by the Ministry of Education (NRF-RS-2018-NR031064 and RS-2025–16063688) and by the Industrial Technology Innovation Program

(RS-2024–00435432, Development of hydrogen production technology through ammonia decomposition using *a* plasmonics-based light system with high performance and long-term durability) funded By the Ministry of Trade Industry & Energy(MOTIE, Korea). D.J. gratefully acknowledge support from Department of Chemistry, College of Natural Science at Jeonbuk National University.

Appendix A. Supporting information

Supplementary data associated with this article can be found in the online version at doi:10.1016/j.nanoen.2025.111632.

Data availability

Data will be made available on request.

References

[1] Y.T. Jiao, J. Dai, Z.H. Fan, J.Y. Cheng, G.P. Zheng, L. Grema, J.W. Zhong, H.F. Li, D.W. Wang, Overview of high-entropy oxide ceramics, Mater. Today 77 (2024) 92–117, https://doi.org/10.1016/j.mattod.2024.06.005.

[2] S.C. Karthikeyan, S. Ramakrishnan, S. Prabhakaran, M.R. Subramaniam, M. Mamlouk, D. Kim, D.J. Yoo, Low-cost self-reconstructed high entropy oxide as an ultra-durable OER electrocatalyst for anion exchange membrane water electrolyzer, Small 20 (2024) 2402241, https://doi.org/10.1002/smll.202402241.

[3] Y. Pu, D. Moseley, Z. He, K.C. Pitike, M.E. Manley, J. Yan, V.R. Cooper, V. Mitchell, V.K. Peterson, B. Johannessen, R.P. Hermann, P. Cao, Mg,Mn,Fe,Co,Ni)O: a rocksalt high-entropy oxide containing divalent Mn and Fe, Sci. Adv. 9 (2023) eadi8809, https://doi.org/10.1126/sciadv.adi8809.

[4] C. Liu, D. Zhang, W. Li, J.A. Trindell, K.A. King, S.R. Bishop, J.D. Sugar, A. H. McDaniel, A.I. Smith, P.A. Salinas, Manganese-based A-site high-entropy perovskite oxide for solar thermochemical hydrogen production, J. Mater. Chem. A 12 (2024) 3910–3922, https://doi.org/10.1039/D3TA03554A.

[5] J.L. Rowell, M. Kang, D. Yoon, K.Z. Jiang, Y. Jia, H.D. Abruña, D.A. Muller, R. D. Robinson, Colloidal synthesis of monodisperse high-entropy spinel oxide nanocrystals, J. Am. Chem. Soc. 146 (2024) 17613–17617, https://doi.org/10.1021/jacs.4c04744.

[6] J. Baek, M.D. Hossain, P. Mukherjee, J. Lee, K.T. Winther, J. Leem, Y. Jiang, W. C. Chueh, M. Bajdich, X. Zheng, Synergistic effects of mixing and strain in high entropy spinel oxides for oxygen evolution reaction, Nat. Commun. 14 (2023) 5936, https://doi.org/10.1038/s41467-023-41359-7.

[7] R.R. Katzbaer, F.M. dos Santos Vieira, I. Dabo, Z. Mao, R.E. Schaak, Band gap narrowing in a high-entropy spinel oxide semiconductor for enhanced oxygen evolution catalysis, J. Am. Chem. Soc. 145 (2023) 6753–6761, https://doi.org/10.1021/jacs.2c12887.

[8] L. An, H. Zhang, J. Zhu, S. Xi, B. Huang, M. Sun, Y. Peng, P. Xi, C.H. Yan, Balancing activity and stability in spinel cobalt oxides through geometrical sites occupation towards efficient electrocatalytic oxygen evolution, Angew. Chem. Int. Ed. 62 (2023) e202214600, https://doi.org/10.1002/anie.202214600.

[9] J. Mei, X. Cheng, Q. Wu, Dual-doped spinel nickel-iron oxide nanoflowers for remarkably enhanced oxygen evolution reaction, J. Alloy. Compd. 1010 (2025) 177292, https://doi.org/10.1016/j.jallcom.2024.177292.

[10] X. He, T. Qiao, B. Li, Z. Zhang, S. Wang, X. Wang, H. Liu, Tuning electronic structure of $CuCo_2O_4$ spinel via Mn-doping for enhancing oxygen evolution reaction, ChemElectroChem 10 (2023) e202200933, https://doi.org/10.1002/celc.202200933.

[11] Y. Yuan, Z. Jiang, M. Li, K. Peng, Magnetic field enhancing the electrocatalytic oxygen evolution reaction of FeMn-based spinel oxides, ACS Appl. Energy Mater. 6 (2023) 7865–7876, https://doi.org/10.1021/acsaem.3c00762.

[12] C. Feng, Y. Zhou, M. Chen, L. Zou, X. Li, X. An, Q. Zhao, P. Xiaokaiti, A. Abudula, K. Yan, High-entropy spinel $(FeCoNiMnAl)_3O_4$ with three-dimensional microflower structure for stable seawater oxidation, Appl. Catal. B Environ. 349 (2024) 123875, https://doi.org/10.1016/j.apcatb.2024.123875.

[13] J.J. Lee, J. Lee, S. Prabhakaran, Y. Lee, D.H. Kim, M.H. Kim, Modulating lattice entropy of rutile $Ru_{0.28}Ir_{0.16}Cr_{0.28}Mn_{0.28}O_2$ nanostructures expedites pH-universal oxygen evolution kinetics, Nano Energy 144 (2025) 111345, https://doi.org/10.1016/j.nanoen.2025.111345.

[14] S.-Y. Lei, L.-B. Liu, S. Liu, W. Sun, Y. Yang, J.-L. Luo, Constructing defect-rich CoO post smart Li extraction from spent Li-ion battery toward efficient oxygen evolution reaction, Chem. Eng. J. 503 (2025) 158325, https://doi.org/10.1016/j.cej.2024.158325.

[15] S. Xin, Y. Tang, B. Jia, Z. Zhang, C. Li, R. Bao, C. Li, J. Yi, J. Wang, T. Ma, Coupling adsorbed evolution and lattice oxygen mechanism in Fe-$Co(OH)_2$/Fe_2O_3 heterostructure for enhanced electrochemical water oxidation, Adv. Funct. Mater. 33 (2023) 2305243, https://doi.org/10.1002/adfm.202305243.

[16] V.A. Mints, K.L. Svane, J. Rossmeisl, M. Arenz, Exploring the high-entropy oxide composition space: Insights through comparing experimental with theoretical models for the oxygen evolution reaction, ACS Catal. 14 (2024) 6936–6944, https://doi.org/10.1021/acscatal.3c05915.

[17] S. Tang, W. Shuang, Y. Wu, Z. Jia, Z. Bai, L. Yang, 3d-orbital overlap modulated d-band center of high-entropy oxyhydroxide for efficient oxygen evolution reaction, Appl. Surf. Sci. 682 (2025) 161760, https://doi.org/10.1016/j.apsusc.2024.161760.

[18] J. Li, Oxygen evolution reaction in energy conversion and storage: Design strategies under and beyond the energy scaling relationship, NanoMicro Lett. 14 (2022), https://doi.org/10.1007/s40820-022-00857-x.

[19] L. Gao, X. Cui, C.D. Sewell, J. Lib, Z. Lin, Recent advances in activating surface reconstruction for the high-efficiency oxygen evolution reaction, Chem. Soc. Rev. 50 (2021) 8428–8569, https://doi.org/10.1039/D0CS00962H.

[20] I.C. Man, H.-Y. Su, F. C.-Vallejo, H.A. Hansen, J.I. Martínez, N.G. Inoglu, J. Kitchin, T.F. Jaramillo, J.K. Nørskov, J. Rossmeisl, Universality in oxygen evolution electrocatalysis on oxide surfaces, ChemCatChem 3 (2011) 1159–1165, https://doi.org/10.1002/cctc.201000397.

[21] H. Jun, E. Kang, J. Moon, H. Kim, S. Han, S. Choung, S. Kim, S.Y. Yi, E. Kang, C. H. Choi, J.W. Han, J. Lee, Quantity effect of heteroatom incorporation on the oxygen evolution mechanism in ruthenium oxide, Chem 11 (2025) 102367, https://doi.org/10.1016/j.chempr.2024.11.005.

[22] N. Luo, A. Cai, J. Pei, X. Zeng, X. Wang, N. Yao, Unveiling oxygen vacancy engineering in CoMo-based catalysts for enhanced oxygen evolution reaction activity, Adv. Funct. Mater. 35 (2025) 2425503, https://doi.org/10.1002/adfm.202425503.

[23] A.L. Maulana, S. Han, Y. Shan, P.-C. Chen, C. L.-Pueyo, S. De, K. S.-Arndt, P. Yang, Stabilizing Ru in multicomponent alloy as acidic oxygen evolution catalysts with machine learning-enabled structural insights and screening, J. Am. Chem. Soc. 147 (2025) 10268–10278, https://doi.org/10.1021/jacs.4c16638.

[24] X. Wang, R. Lu, S. Gong, S. Yang, W. Wang, Z. Sun, X. Zhang, J. Liu, X. Lv, Identification of the reconstruction induced high-entropy spinel oxide nanosheets for boosting alkaline water oxygen evolution, Chem. Eng. J. 503 (2025) 158488, https://doi.org/10.1016/j.cej.2024.158488.

[25] X. Tian, R. Liu, W. Wang, Q. Yang, Z. Huang, Y. Yang, J. Han, T. Dong, Y. Du, J. Lai, H. Li, L. Wang, 3D ordered macroporous superstructures of high entropy hydroxide with strong orbital coupling enhancing water/seawater oxidation, Adv. Mater. (2025) e06068, https://doi.org/10.1002/adma.202506068.

[26] M.V. Kante, M.L. Weber, S. Ni, I.C.G. van den Bosch, E. van der Minne, L. Heymann, L.J. Falling, N. Gauquelin, M. Tsvetanova, D.M. Cunha, G. Koster, F. Gunkel, S. Nemšák, H. Hahn, L.V. Estrada, C. Baeumer, A high-entropy oxide as high-activity electrocatalyst for water oxidation, ACS Nano 17 (2023) 5329–5339, https://doi.org/10.1021/acsnano.2c08096.

[27] W. Hooch Antink, S. Lee, H.S. Lee, H. Shin, T.Y. Yoo, W. Ko, J. Shim, G. Na, Y.-E. Sung, T. Hyeon, High-valence metal-driven electronic modulation for boosting oxygen evolution reaction in high-entropy spinel oxide, Adv. Funct. Mater. 34 (2024) 2309438, https://doi.org/10.1002/adfm.202309438.

[28] G. Kresse, J. Furthmüller, Efficient iterative schemes for ab initio total-energy calculations using a plane-wave basis set, Phys. Rev. B 54 (1996) 11169–11186, https://doi.org/10.1103/PhysRevB.54.11169.

[29] G. Kresse, J. Furthmüller, Efficiency of ab-initio total energy calculations for metals and semiconductors using a plane-wave basis set, Comput. Mater. Sci. 6 (1996) 15–50, https://doi.org/10.1016/0927-0256(96)00008-0.

[30] G. Kresse, D. Joubert, From ultrasoft pseudopotentials to the projector augmented-wave method, Phys. Rev. B 59 (1999) 1758–1775, https://doi.org/10.1103/PhysRevB.59.1758.

[31] J.P. Perdew, K. Burke, M. Ernzerhof, Generalized gradient approximation made simple, Phys. Rev. Lett. 77 (1996) 3865–3868, https://doi.org/10.1103/PhysRevLett.77.3865.

[32] S. Grimme, J. Antony, S. Ehrlich, H. Krieg, A consistent and accurate ab initio parametrization of density functional dispersion correction (DFT-D) for the 94 elements H-Pu, J. Chem. Phys. 132 (2010) 154104, https://doi.org/10.1063/1.3382344.

[33] S. Grimme, Accurate description of van der Waals complexes by density functional theory including empirical corrections, J. Comput. Chem. 25 (2004) 1463–1473, https://doi.org/10.1002/jcc.20078.

[34] S. Grimme, S. Ehrlich, l Goerigk, Effect of the damping function in dispersion corrected density functional theory, J. Comp. Chem. 32 (2011) 1456–1465, https://doi.org/10.1002/jcc.21759.

[35] P.E. Blöchl, Projector augmented-wave method, Phys. Rev. B 50 (1994) 17953–17979, https://doi.org/10.1103/PhysRevB.50.17953.

[36] H.J. Monkhorst, J.D. Pack, Special points for Brillouin-zone integrations, Phys. Rev. B 13 (1976) 5188–5192, https://doi.org/10.1103/PhysRevB.13.5188.

[37] D.C. Ghosh, R. Biswas, Theoretical calculation of absolute radii of atoms and ions. Part 2. The ionic radii, Int. J. Mol. Sci. 4 (2003) 379–407, https://doi.org/10.3390/i4060379.

[38] T. Chuang, C. Brundle, D. Rice, Interpretation of the X-ray photoemission spectra of cobalt oxides and cobalt oxide surfaces, Surf. Sci. 59 (1976) 413–429, https://doi.org/10.1016/0039-6028(76)90026-1.

[39] G.P. Halada, C.R. Clayton, Photoreduction of hexavalent chromium during X-ray photoelectron spectroscopy analysis of electrochemical and thermal films, J. Electrochem. Soc. 138 (1991) 2921, https://doi.org/10.1149/1.2085340.

[40] E. Agostinelli, C. Battistoni, D. Fiorani, G. Mattogno, M. Nogues, An XPS study of the electronic structure of the $Zn_xCd_{1-x}Cr_2$ (x= S, Se) spinel system, J. Phys. Chem. Solids 50 (1989) 269–272, https://doi.org/10.1016/0022-3697(89)90487-3.

[41] Y. Abe, K. Kato, M. Kawamura, K. Sasaki, Rhodium and rhodium oxide thin films characterized by XPS, Surf. Sci. Spectra 8 (2001) 117–125, https://doi.org/10.1116/11.20010801.

[42] T. Yamashita, P. Hayes, Analysis of XPS spectra of Fe^{2+} and Fe^{3+} ions in oxide materials, Appl. Surf. Sci. 254 (2008) 2441–2449, https://doi.org/10.1016/j.apsusc.2007.09.063.

[43] J. Yin, P. Zhou, L. An, L. Huang, C. Shao, J. Wang, H. Liu, P. Xi, Self-supported nanoporous $NiCo_2O_4$ nanowires with cobalt–nickel layered oxide nanosheets for overall water splitting, Nanoscale 8 (2016) 1390–1400, https://doi.org/10.1039/C5NR06197K.

[44] D. Wang, S. Jiang, C. Duan, J. Mao, Y. Dong, K. Dong, Z. Wang, S. Luo, Y. Liu, X. Qi, Spinel-structured high entropy oxide $(FeCoNiCrMn)_3O_4$ as anode towards superior lithium storage performance, J. Alloy. Compd. 844 (2020) 156158, https://doi.org/10.1016/j.jallcom.2020.156158.

[45] S. Kumar, K. Kumari, A. Kumar, B. Koo, A. Vij, Chapter 28-Raman spectroscopy of spinel ferrites. Ferrite Nanostructured Magnetic Materials, Woodhead Publishing, 2023, pp. 537–555, https://doi.org/10.1016/B978-0-12-823717-5.00041-3.

[46] L. Danyang, S. Liping, L. Qiang, X. Tian, H. Lihua, Z. Hui, High-entropy oxide $(Fe_{0.2}Zn_{0.2}Co_{0.2}Ni_{0.2}Cu_{0.2})Fe_2O_4$: An efficient and stable spinel-type electrocatalyst for H_2O_2 production in alkaline media, J. Alloy. Compd. 913 (2022) 165148, https://doi.org/10.1016/j.jallcom.2022.165148.

[47] Z. Lazarević, Č. Jovalekić, D. Sekulić, M. Slankamenac, M. Romčević, A. Milutinović, N. Romčević, Characterization of nanostructured spinel $NiFe_2O_4$ obtained by soft mechanochemical synthesis, Sci. Sinter. 44 (2012) 331–339, https://doi.org/10.2298/SOS1203331L.

[48] N. Bahlawane, P.H.T. Ngamou, V. Vannier, T. Kottke, J. Heberle, K. Kohse-Höinghaus, Tailoring the properties and the reactivity of the spinel cobalt oxide, Phys. Chem. Chem. Phys. 11 (2009) 9224–9232, https://doi.org/10.1039/B910707J.

[49] B. Nandan, M. Bhatnagar, S.C. Kashyap, Cation distribution in nanocrystalline cobalt substituted nickel ferrites: X-ray diffraction and Raman spectroscopic investigations, J. Phys. Chem. Solids 129 (2019) 298–306, https://doi.org/10.1016/j.jpcs.2019.01.017.

[50] O. van der Heijden, S. Park, R.E. Vos, J.J.J. Eggebeen, M.T.M. Koper, Tafel slope plot as a tool to analyze electrocatalytic reactions, ACS Energy Lett. 9 (2024) 1871–1879, https://doi.org/10.1021/acsenergylett.4c00266.

[51] J.K. Nørskov, F. Abild-Pedersen, F. Studt, T. Bligaard, Density functional theory in surface chemistry and catalysis, Proc. Natl. Acad. Sci. 108 (2011) 937–943, https://doi.org/10.1073/pnas.100665210.

[52] Y. Xu, F. Zhang, T. Sheng, T. Ye, D. Yi, Y. Yang, S. Liu, X. Wang, J. Yao, Clarifying the controversial catalytic active sites of Co_3O_4 for the oxygen evolution reaction, J. Mater. Chem. A 7 (2019) 23191–23198, https://doi.org/10.1039/C9TA08379K.